Electrochimica Acta 270 (2018) 440–452

Contents lists available at ScienceDirect

Electrochimica Acta

journal homepage: www.elsevier.com/locate/electacta

Modeling of degradation effects and its integration into electrochemical reduced order model for Li(MnNiCo)O_2/Graphite polymer battery for real time applications

Yinyin Zhao [a], Song-Yul Choe [a, *], Jungdo Kee [b]

[a] Mechanical Engineering, Auburn Univ., 1418 Wiggins Hall, AL 36849, USA
[b] Central Advanced Research and Engineering Institute, Hyundai-Kia Motors Corporate R&D Division, South Korea

ARTICLE INFO

Article history:
Received 28 September 2017
Received in revised form
1 January 2018
Accepted 16 February 2018
Available online 19 February 2018

Keywords:
Lithium ion polymer battery
Reduced order model
Degradation effects
Side reaction
Solid electrolyte interphase (SEI)

ABSTRACT

Previously, a highly efficient reduced order model (ROM) for Li(MnNiCo)O_2/Graphite polymer battery based on electrochemical principles has been developed for real time applications. The execution time is significantly reduced compared to that of the electrochemical thermal full order model while beginning of life of the battery with the approximately same accuracy can be predicted. However, prediction of the end of life associated with degradation effects of battery was not included. Our investigations on aging mechanisms of the Li(MnNiCo)O_2 (MNC) lithium ion batteries have revealed that side reaction is the main cause among others for capacity and power fade of the battery. The production of the side reaction forms thin unsolvable layers that adhere to the surface of the graphite particles and grow as cycled, which is called solid electrolyte interphase (SEI). Growth of the SEI leads to loss of the lithium ions, loss of the electrolytes and loss of the active volume fraction. These effects are described using the Butler-Volmer kinetics and aging parameters. Particularly, electrolyte solvent diffusion described by Fick's law is integrated into the degradation model, which results in quantifying the electrolyte solvent concentration in SEI. The exchange current density of the side reaction is formulated as a function of electrolyte solvent and lithium ion concentration, which justifies the reaction rate in the aspect of reactants. In addition, temperature dependency of the model parameters is also considered by adopting the energy equations. Finally, the degradation model is incorporated into the ROM.

Performances of the integrated ROM are compared with the experimental data collected from a high power pouch type lithium ion polymer battery with Li [MnNiCo]O_2/Graphite chemistry.

1. Introduction

Lithium ion batteries have been widely adopted as energy storage for different power systems due to their high power and energy density. The safety and reliability of the battery operations are ensured by battery management system (BMS) that monitors overcharge and undercharge of batteries using state of charge and health estimated based on model. The model can be constructed using equivalent electric circuit or electrochemical thermal principles [1]. Computation of the responses of the battery using electrochemical models is performed numerically, which requires high computational time. As a result, the model is not appropriate for real time applications. Recently, we proposed a highly efficient reduced order model (ROM) based on the electrochemical and thermal principles for real time applications [2]. The ROM employed different model reduction techniques that include Padé approximation, residue grouping, proper orthogonal decomposition and linearization, so the computational time has been substantially reduced compared to that of the electrochemical thermal full order model, while the accuracy is still maintained. However, the developed ROM can only predict the responses at beginning of life of batteries. Lacking of aging effects in the model limits its practical uses for BMS, particularly in estimation of capacity and power fade. Degradation of performance of batteries is primarily induced by operating conditions and results in production of byproducts, morphology changes of electrodes and ion diffusivity of electrolyte.

The major causes and effects for degradation are summarized in Table 1.

* Corresponding author.
E-mail addresses: yzz0031@tigermail.auburn.edu (Y. Zhao), choe@auburn.edu (S.-Y. Choe), jdkee@hyundai.com (J. Kee).

https://doi.org/10.1016/j.electacta.2018.02.086
0013-4686/

Nomenclature

A	sandwich area of the cell (cm^2)
a_s	specific surface area of electrode (cm^{-1})
c	ion concentration (mol L^{-1})
D	diffusion coefficient(cm^2 s^{-1})
F	Faraday constant (96,487 C mol^{-1})
I	current of the cell (A)
i_0	exchange current density of intercalation (Acm^{-2})
j^{Li}	reaction rate of intercalation (Acm^{-3})
k_{iso}	isolation coefficient due to SEI
L	thickness of the micro cell (cm)
MNC	$Li(MnNiCo)O_2$
OCV	open circuit voltage (V)
Q	capacity of the cell (Ah)
q	amount of ion loss caused by the side reaction (Ah)
R	resistance (Ω cm^2) or universal gas constant (8.3143 J mol^{-1} K^{-1})
R_s	radius of spherical electrode particle (cm)
r	coordinate along the radius of electrode particle (cm)
SOC	state of charge
SEI	solid electrolyte interphase
T	cell temperature (K)
t	time (s)
U	potential (V)
V	voltage (V) or volume of the composite electrode (cm^3)
$\overline{V}$	molar volume (cm^3 mol^{-1})
x	stoichiometric number of the anode
y	stoichiometric number of the cathode

Greek symbols

α	transfer coefficient for an electrode reaction
δ	thickness (cm)
ε	volume fraction of a porous medium
ϕ	Finite element method (FEM) solution of potentials
η	surface overpotential of electrode reaction (V)
κ	ionic conductivity of electrolyte (S cm^{-1})
σ	conductivity (S cm^{-1})

Subscripts and superscripts

a	anodic
ave	average value
c	cathodic
D	diffusion
EC	ethylene carbonate
e	electrolyte phase
eff	effective
$equi$	equilibrium
Li	Lithium ion
main	main reaction
max	maximum
r	radial direction in electrode particle
s	solid phase
sep	separator
$side$	side reaction
$surf$	electrode particle surface
T	terminal
0%	0% SOC
100%	100% SOC
+	positive electrode (cathode)
-	negative electrode (anode)

Among the aging causes, the side reaction taking place at the anode graphite particle surfaces is the most predominant cause of the battery degradation. The main reaction is the process that lithium ions intercalate and de-intercalate on the surface of the electrode particles when cycling. In contrast, the side reaction refers to the electrolyte decomposition reaction that is sustained slowly but constantly throughout the battery life. It is particularly severe during charging process when the anode is polarized and its potential becomes low, which is then stimulated by elevated temperature and high SOC range [3].

The side reaction consumes lithium ions as well as solvents of electrolyte, and produces deposits that form thin unsolvable layers that adhere to the surface of the anode graphite particles. A schematic diagram reproduced from Ref. [4] below in Fig. 1 shows the main and side reaction that take place concurrently at the anode graphite particle surface and the formation of the solid electrolyte interphase (SEI).

Several possible reaction mechanisms and products dependent upon various electrolyte solvent mixtures are reported in the literature [5,6]. Since ethylene carbonate (EC) is the organic solvent used for the electrolyte of the investigated batteries, only two predominant side reactions as shown below are considered [5]:

$$2Li^+ + 2e^- + EC \rightarrow CH_2 = CH_2 + Li_2CO_3 \downarrow \quad (1)$$

Table 1
Summary of degradation mechanisms.

Components	Major causes	Effects and consequences	Enhanced by
Graphite particle anode	• Side reaction (electrolyte solvent decomposition)	• SEI formation • Loss of lithium ion • Loss of active material • Increase of impedance • Gas generation and particle cracking • Corrosion of current collector • Self-discharge	• High temperature • High SOC range
	• Low temperature operation • Overcharge	• Lithium plating • Loss of lithium ion (Loss of electrolyte in subsequent reaction with Li metal)	• Low temperature • High charge rate
Separator (electrolyte)	• Side reaction	• SEI formation • Loss of electrolyte	• High temperature • High SOC range
Metal oxide cathode	• Mechanical stress and strain	• Phase transition and structural changes • Cracking and fracture	• High temperature

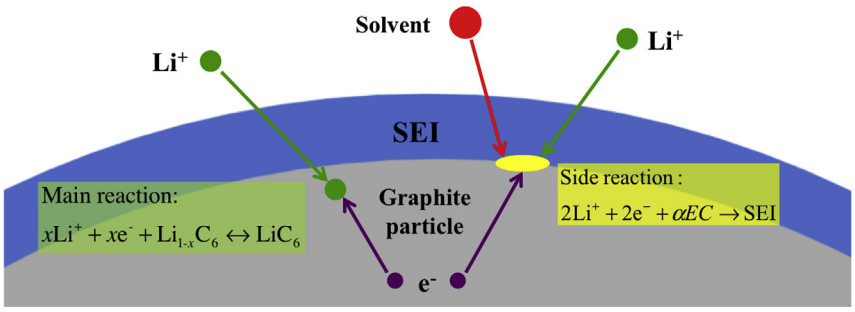

Fig. 1. Schematic diagram of the main and side reaction on graphite particles.

$$2Li^+ + 2e^- + 2EC \rightarrow CH_2 = CH_2 + (CH_2OCO_2Li)_2 \downarrow \quad (2)$$

It is shown that the first reaction requires 1 mol of EC while the second reaction requires 2 mol to produce 1 mol of deposit. Accordingly, the major composition of SEI for the EC based lithium ion batteries is a combination of lithium carbonate (Li_2CO_3) and lithium ethylene dicarbonate ($(CH_2OCO_2Li)_2$). The ratio of both compounds is dependent on the concentration of EC in electrolyte [5].

In fact, the SEI layer is ion conductive with low solvent permeability, but nonconductive to electrons. Therefore, the initial formation of SEI serves as a crucial passivation layer that protects the charged negative electrode from corrosion and prevents the electrolyte from further reduction. The initially formed SEI can be regarded as the "good SEI".

However, the pores present in the SEI layer allow for the electrolyte solvent molecules to diffuse through the existing SEI layer with a small but persistent rate. Finally, the molecules react with lithium ions at the interface between the existing SEI layer and the graphite particle, which leads to formation of a new deposit that continuously grows, as depicted in Fig. 1. The continuously grown SEI layer can be regarded as the "bad SEI".

Volume changes of the electrode particles during lithium ion intercalation/de-intercalation processes induce cracks in SEI and potentially fractures. Another new SEI layer can be formed at the cracks of the existing SEI [6]. However, this effect is not considered in this paper.

As the deposits caused by side reaction are accumulated with prolonged cycles, the thickness of SEI grows gradually. As a result, the ionic resistance of the SEI increases, which results in power fade. Previous study has shown that large amount of deposits are particularly produced at the interface between the composite anode and the separator [7], because the side reaction rate near the separator is larger than that inside of the electrode particles. This thick deposit in this area form a "deposit layer" that has the same composition as those in the SEI layer. The deposits can clog the pores of the particles that decrease the accessible surface of the active material for charges. At the extreme case, some of the particles that fully covered by the deposits become electrically isolated from other particles, so participation in chemical reaction is not possible.

Lithium ions that have been trapped in the isolated particles, along with those consumed in the side reaction, attribute to total ion loss and consequently the capacity fade. Additionally, the irreversible side reaction also consumes electrolyte solvent, which results in the decrease of the electrolyte volume fraction and consequently the ion conductivity in the electrolyte.

The effects of the side reaction are summarized with respect to the reactants versus the products in Table 2.

There have been numerous attempts to model degradation phenomenon and predict lifetime of a battery. The models can be categorized into two groups based on either empirical equation or physical equation. The models in the first group extract the empirical relationship between the aging parameters and the cycling or storage time based on the experimental data. The coefficients of the empirical equations are determined by fitting the simulation curves obtained by a physics-based model that is embedded with the empirical equations to the experimental data. For the first time, a relationship between the consumption of lithium ions and the growth of SEI was proposed under the assumption that loss of lithium ions is proportional to the SEI conductivity [8], which results in a square root function between the SEI thickness and time. This function was further extended to describe the relationship between the capacity and the film resistance with respect to time [9]. Moreover, the active surface area of electrodes, as well as the initial SOC was considered by the curve fittings [10]. Diffusion coefficients were also added into the group of parameters affected by battery aging [11]. Additionally, control techniques were employed to improve the prediction performance [12].

The models based on empirical equation are straightforward but heavily rely on experiments that are limited in reality. Therefore, these empirical models cannot fully cover all range of operations till the end of life of battery. Consequently, this approach is time consuming and costly and its performance is relatively vulnerable to changed operating conditions.

Models in the second group are constructed considering the side reaction. The side reaction is described by modified Butler-Volmer (BV) equation that quantifies the reaction rate and facilitates analysis of the aging processes and prediction of the aging parameters. The modified BV equation for the side reaction was firstly introduced to describe the solvent reduction reaction [13]. A proportional relationship between the increasing rate of the SEI thickness and the side reaction rate was proposed. Then, the concentration gradient of EC along the SEI thickness direction is corrected by embedding the mass balance equation of the electrolyte solvent in the SEI layer [14]. Additionally, correlation between the side reaction rate and the electrode active material volume fraction was derived and used to update the values of the active surface area and the diffusion coefficients [15]. Subsequently, the solvent diffusion model with corrected boundary conditions and BV equation were incorporated into a single particle model [16]. Furthermore, the expression of the EC concentration is simplified and extended to the porous electrode model [4]. Effects of the deposit layer on the ionic conductivity and the change of volume fraction considering porosity were then discussed [17]. Studies have shown that models based on the BV equations are complex but accurate for explicitly describing the side reaction processes with solid physical principles. However, the mass balance of the electrolyte solvent, as well as the relationship between the

Table 2
Summary of side reaction effects.

By reactants	By products

• Loss of lithium ion
• Loss of electrolyte
  • Decrease of electrolyte volume fraction
  • Decrease of lithium ion diffusivity in electrolyte
	• Growth of SEI thickness and deposit layer
	  • Increase of SEI resistance
	  • Decrease of ionic conductivity
	• Loss of active material in anode
	  • Decrease of electrode volume fraction due to blocking pores
	  • Loss of electronic contact due to isolated graphite particles

exchange current density and the solvent concentration, has never been applied in the porous electrode model. In addition, integration and experimental validation of the degradation phenomenon in a ROM have never been conducted in the literature. Therefore, the aging phenomena and their modeling can be further improved by considering following aspects;

1) Integration of the mass balance of electrolyte solvent into the porous electrode model with side reaction rate as the source term in the boundary conditions.
2) The exchange current density as a function of lithium ion concentration and the EC concentration on the electrode particle surfaces.
3) The diffusion coefficients dependent upon temperature.
4) Extensive validations of the aging model against experimental data under various operating conditions.

2. ROM and degradation model

2.1. ROM

A pouch type lithium ion polymer single cell is constructed by stacked layers of electrode, current collector and separator, where the current collectors are connected to increase energy density. In order to model the cell's behavior, the cell is reduced to a microcell that has a sandwich structure in the thickness direction, which is composed of a separator in the middle with two composite electrodes. The composite electrode is a mixture of active material, electrolyte and binder. The particles dispersed on electrodes are modeled as spheres that are uniformly distributed. A schematic diagram for this microcell is depicted in Fig. 2, where the active material on the anode is the graphite particles and that on the cathode is the metal oxides. When a cell is discharging or charging, ions are transported through electrolyte and chemically react at active materials, diffuse in the solid, finally rested after

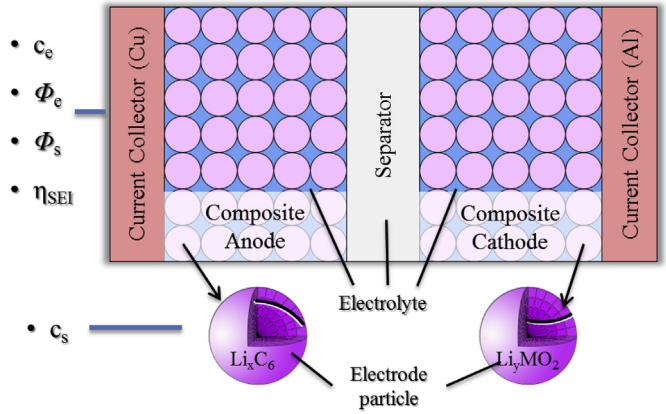

Fig. 2. Schematic diagram of a model for a pouch type single cell.

intercalation in a lattice structure. Meanwhile, electrons flow through an external circuit and complete the redox processes.

Ion transport, chemical reaction, diffusion process and finally intercalation and de-intercalation are governed by a set of coupled partial differential equations that describe ion and charge conservation in electrode and electrolyte, and electrochemical kinetics is formulated by Butler-Volmer equation. There are four key variables in the governing equations, ion concentrations and potentials in electrode and electrolyte, which are numerically solved using the finite volume methods in the Full Order Model (FOM). The FOM can be used to accurately calculate values at each grid point, but is inappropriate for real time applications because of high computation time. One of methods for reduction of the calculation time is to mathematically simplify the governing equations, which is called reduced order model (ROM) that is commonly derived from the FOM. In the previous work, a highly efficient ROM is derived and proposed for real time applications [2]. The results have showed that the proposed ROM reduces the computational time at least to one-tenth of that of FOM while overall accuracies can be maintained. The governing equations for FOM and the corresponding model reduction techniques used for ROM are summarized in Table 3.

2.2. Degradation model

For development of a degradation model, several assumptions have been made:

- The side reaction is irreversible and no overcharge is considered.
- Only the solvent decomposition that takes place at the anode is considered as the source for degradation.
- Electrode volume changes, structure deformations and graphite particle cracks caused by internal mechanical stress are neglected.
- Composition of SEI is a mixture of Li_2CO_3 and $(CH_2OCO_2Li)_2$, which are the products of the side reaction (1) and (2) with the same reaction rate [17].

2.2.1. Main reaction and side reaction

For the previously developed FOM or ROM, the BV equation only describes the charge transfer processes for the main reaction on the electrode graphite particle surfaces. When considering the aging processes, the total reaction rate is a sum of the main and the side reaction, and the overall BV kinetic expression for the anode becomes as follows,

$$j^{Li} = j^{Li}_{main} + j^{Li}_{side} \tag{3}$$

where $j^{Li}, j^{Li}_{main}, j^{Li}_{side}$ denote the total reaction rate, the main reaction rate and the side reaction rate, respectively.

The main reaction rate is the current density caused by the chemical reaction that takes place at the interface between the electrode graphite particle surfaces and the SEI layer. The

Table 3
Governing equations for FOM and applied techniques for ROM.

	FOM	ROM
Ion conservation in electrode	$\frac{\partial C_s}{\partial t} = \frac{D_s}{r^2}\frac{\partial}{\partial r}\left(r^2\frac{\partial C_s}{\partial r}\right)$ $\left.\frac{\partial C_s}{\partial r}\right\|_{r=0} = 0$ B.C. $D_s\left.\frac{\partial C_s}{\partial r}\right\|_{r=R_s} = -\frac{j^{Li}}{a_s F}$	Padé approximation $\frac{C_{s,surf}(s)}{j^{Li}(s)} = \frac{a_0+a_1 s+\cdots a_{Q-1}s^{Q-1}}{s(1+b_2 s+\cdots b_Q s^{Q-1})}\frac{C_{s,ave}(s)}{j^{Li}(s)} = -\frac{3}{R_s a_s F s}$
Ion conservation in electrolyte	$\frac{\partial(\varepsilon_e C_e)}{\partial t} = \frac{\partial}{\partial x}\left(D_e^{eff}\frac{\partial}{\partial x}C_e\right) + \frac{1-t^0}{F}j^{Li}$ B. C. $\left.\frac{\partial C_e}{\partial x}\right\|_{x=0} = \left.\frac{\partial C_e}{\partial x}\right\|_{x=L} = 0$	Residue Grouping $A^* = diag[\lambda_1 \quad \lambda_2 \quad \cdots \quad \lambda_N]\, B^* = [1 \quad 1 \quad \cdots \quad 1]C = [\vec{r}_1\lambda_1 \quad \vec{r}_2\lambda_2 \quad \cdots \quad \vec{r}_N\lambda_N]D = [Z + \sum_{f=1}^{N}\vec{r}_f]$
Charge conservation in electrode	$\frac{\partial}{\partial x}\left(\sigma^{eff}\frac{\partial}{\partial x}\varphi_s\right) - j^{Li} = 0$ $-\sigma_-^{eff}\left.\frac{\partial \varphi_s}{\partial x}\right\|_{x=0} = -\sigma_+^{eff}\left.\frac{\partial \varphi_s}{\partial x}\right\|_{x=L} = \frac{I}{A}$ B. C. $\left.\frac{\partial \varphi_s}{\partial x}\right\|_{x=L_-} = \left.\frac{\partial \varphi_s}{\partial x}\right\|_{x=L_-+L_{sep}} = 0$	Proper Orthogonal Decomposition (POD) $[U \quad \Sigma \quad V] = svd(\vec{\varphi}_{full}^{T}\cdot\vec{\varphi}_{full})$ $A(\Phi\cdot\vec{a}) = b$ $\Phi = U(:, 1{:}N)$ $\vec{a} = \Phi^T A^{-1} b$
Electrochemical Kinetics	Butler-Volmer (BV) equation: $j^{Li} = a_s i_0\left(\exp\left(\frac{\alpha_a F}{RT}\eta\right) - \exp\left(-\frac{\alpha_c F}{RT}\eta\right)\right)$	Linearization $j^{Li} = a_s i_0 \frac{(\alpha_a+\alpha_c)F}{RT}\eta$
Equilibrium potentials	Active overpotential: $\eta = \varphi_s - \varphi_e - U_{equi}$ $U_-(x) = U_-^0(x) + \frac{RT}{nF}\ln\left(\frac{C_e^-}{C_e^0}\right),\ U_-(x) = U_-^0(x) when C_e^- = C_e^0 at\ equilibrium\ state.$ $U_+(x) = U_+^0(x) + \frac{RT}{nF}\ln\left(\frac{C_e^+}{C_e^0}\right),\ U_+(x) = U_+^0(x) when C_e^+ = C_e^0 at\ equilibrium\ state.$ $U_-^0(x) = -1.8636x^5 + 6.6478x^4 - 9.07126x^3 + 5.7843x^2 - 1.7970x + 0.3294$ $U_+^0(y) = -1550.039y^7 + 6806.298y^6 - 12633.679y^5 + 12829.327y^4 - 7687.388y^3 + 2715.077y^2 - 523.437y + 46.682$ $x = C_{s,surf\_}/C_{s,max\_}$ $y = C_{s,surf_+}/C_{s,max\_}$	

corresponding BV equation composed of oxidation and reduction process is expressed as follows:

$$j_{main}^{Li} = a_s i_{0,main}\left(\exp\left(\frac{\alpha_{a,main}\cdot F}{RT}\eta_{main}\right) - \exp\left(-\frac{\alpha_{c,main}\cdot F}{RT}\eta_{main}\right)\right) \tag{4}$$

where a_s is the specific reaction area and $i_{0,main}$ is the exchange current density and it is related both electrode particle surface and electrolyte concentrations according to $i_0 = k(c_e)^{\alpha_{a,main}}(c_{s,\max} - c_{s,surf})^{\alpha_{a,main}}(c_{s,surf})^{\alpha_{c,main}}$. $\alpha_{a,main}$ and $\alpha_{c,main}$ are the anodic and cathodic charge transfer coefficient of the main reaction, which is assumed to be a values of 0.5. k is a kinetic rate constant.

Equation (4) can be simplified to a linearized form as we described in Table 3 and shown in Equation (5):

$$j_{main}^{Li} = a_s i_{0,main}\frac{(\alpha_{a,main} + \alpha_{c,main})\cdot F}{RT}\eta_{main} \tag{5}$$

By considering the SEI resistance, the activation overpotential of the main reaction η_{main} becomes the following Equation (6):

$$\eta_{main} = \varphi_s - \varphi_e - U_{equi,main} - \frac{R_{SEI}}{a_s}j^{Li} \tag{6}$$

where φ_s and φ_e are the electrical potential of the solid electrodes and electrolyte, respectively. R_{SEI} is the ionic resistance of the SEI layer of particles on the anode side. $U_{equi,main}$ is the equilibrium potential of the main reaction, which is a function of the stoichiometry number that is a fraction of the ion concentration on the particle surface over the maximum concentration.

The equilibrium potential of the anode, U_-, and the equilibrium potential of the cathode, U_+, are approximated by empirical equations shown in Table 3. The summation of U_- and the open circuit voltage (OCV) that measured experimentally is the equilibrium potential U_+. Equilibrium potentials of both electrodes along with the OCV curve are plotted in Fig. 3.

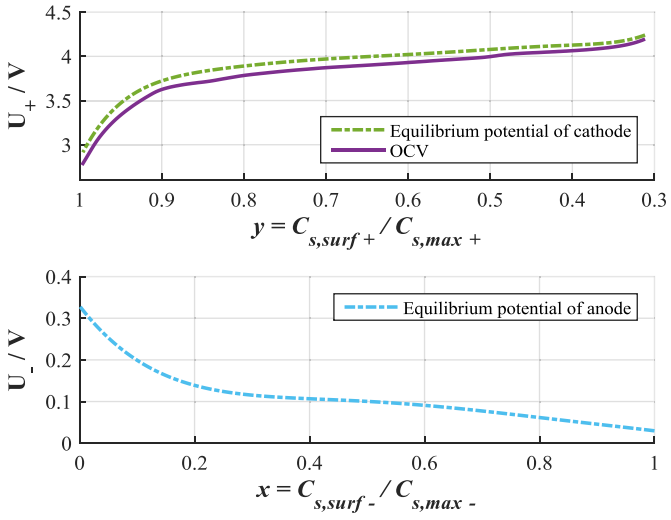

Fig. 3. Open circuit voltage and equilibrium potentials of both electrodes.

Since the side reaction is irreversible because of high reaction rate of the electrolyte solvent reduction compared to that of the oxidation process, the BV equation for the side reaction can be simplified by only containing the reduction part as shown in Equation (7):

$$j_{side}^{Li} = -a_s i_{0,side} \exp\left(-\frac{\alpha_{c,side} n_{side} F}{RT} \eta_{side} \right) \tag{7}$$

where n_{side} is the number of electrons involved in the side reaction and that is equal to two as seen in Equations (1) and (2).

The activation overpotential of the side reaction, η_{side}, can be calculated using Equation (8):

$$\eta_{side} = \varphi_s - \varphi_e - U_{equi,side} - \frac{R_{SEI}}{a_s} j^{Li} \tag{8}$$

where $U_{equi,side}$ is the equilibrium potential of the side reaction. The potential varies dependent upon composition of electrolyte. References recommend different values such as 2V, 1.7V or 1V, but 0.4V [13–16] and 0.8V [4,18–20] are the most widely used practical values. In this work, the value of $U_{equi,side}$ is iteratively fitted using the terminal voltage obtained by the experimental data.

The exchange current density, $i_{0,side}$, is correlated to the concentrations of two reactants of the side reaction, lithium ions and EC molecules. Compared to the exchange current density of the main reaction in Ref. [21], the side reaction exchange current density, $i_{0,side}$, is expressed as follows [4]:

$$i_{0,side} = k_{side} \sqrt{c_{s,surf} \cdot c_{EC,R_s}} \tag{9}$$

where k_{side} is a kinetic rate constant for the side reaction. $c_{s,surf}$ and c_{EC,R_s} are the concentrations of the lithium ions and the EC molecules at the graphite particle surfaces, respectively.

2.2.2. Solvent diffusion

The exchange current density of the side reaction is a function of the concentrations of lithium ions and EC molecules on the graphite particle surface. The lithium ion concentration can be calculated from the ROM. In order to obtain the concentration gradient of the EC molecules along the SEI thickness direction, an additional diffusion equation governed by the Fick's law is used. Since the thickness of the SEI is very thin compared to that of the graphite particle radius, the first derivative term of the Fick's equation can be neglected, so the partial differential equation can be simplified as follows (10):

$$\frac{\partial c_{EC}}{\partial t} = D_{EC} \frac{\partial^2 c_{EC}}{\partial r^2} \tag{10}$$

where D_{EC} is the diffusivity of the EC in the SEI layer. r is the coordinate in the particle radial direction.

This equation describes the EC concentration in the SEI from the surface of the graphite particles to the electrolyte bulk. The outer boundary given by $r = R_S + \delta_{SEI}$ is a variable that includes the growth rate of the SEI thickness. The boundary conditions for Equation (10) are given as follows:

$$-D_{EC} \frac{\partial c_{EC}}{\partial r}\bigg|_{r=R_s} = \frac{j_{side}^{Li}}{a_s F}$$
$$c_{EC}|_{r=R_s+\delta_{SEI}} = c_{EC,bulk} \tag{11}$$

where R_s is the radius of the graphite particles. δ_{SEI} is the thickness of the SEI layer. $c_{EC,bulk}$ is the EC concentration in the electrolyte bulk.

Equation (10) that describe the solvent diffusion in the SEI layer is a partial differential equation (PDE), which can be solved numerically by finite difference method in both time and space domain. The corresponding boundary condition shown in Equation (11) is a function of both time and space. As the SEI layer grows, the boundary is moving as well, which presents Stefan's problem that is solved by the spatial coordinate transformation method [22].

Since the thickness of the SEI layer is much thinner than the radius of the electrode particles, the spherical coordinate of the SEI layer can be replaced with the Cartesian coordinate. Therefore, the radial direction r is transformed to the thickness direction x and the EC concentration $c_{EC}(r,t)$ in the radial direction is transformed to $c_{EC}(x,t)$ in the thickness direction as follows.

$$\frac{\partial c_{EC}}{\partial t} = D_{EC} \frac{\partial^2 c_{EC}}{\partial x^2} \tag{12}$$

Since the newly formed SEI is growing between the existing SEI and the graphite particle surface, the origin of the x-axis should be located at the interface of the electrolyte and the SEI layer. The effective range of the EC diffusion equation is transformed from $R_s < r < R_s + \delta_{SEI}(t)$ to $0 < x < \delta_{SEI}(t)$ and the corresponding boundary conditions are shown in Equation (13).

$$-D_{EC} \frac{\partial c_{EC}}{\partial x}\bigg|_{x=\delta_{SEI}} = \frac{j_{side}^{Li}}{a_s F}$$
$$c_{EC}|_{x=0} = c_{EC,bulk} \tag{13}$$

The spatial coordinate transformation method is used to modify the space grid. The variable of the spatial coordinate, y is constructed by dividing the original coordinate, x by the SEI thickness δ_{SEI} that is a function of time. EC concentration, $c_{EC}(x,t)$, is transformed equivalently to $\tilde{c}_{EC}(y,t)$ as shown in Equation (14).

$$y = \frac{x}{\delta_{SEI}(t)}, \quad \tilde{c}_{EC}(y,t) = c_{EC}(x,t) \tag{14}$$

By substituting Equation (14) into Equations (12) and (13), the original EC diffusion equation and the corresponding moving boundary conditions are reformulated as follows.

$$\frac{\partial \tilde{c}_{EC}}{\partial t} = \frac{D_{EC}}{\delta_{SEI}^2} \frac{\partial^2 \tilde{c}_{EC}}{\partial y^2} \tag{15}$$

$$-\frac{D_{EC}}{\delta_{SEI}} \frac{\partial \tilde{c}_{EC}}{\partial y}\bigg|_{y=1} = \frac{j_{side}^{Li}}{a_s F}$$
$$\tilde{c}_{EC}|_{y=0} = c_{EC,bulk} \tag{16}$$

As a result, the effective range is finally transformed to $0 < y < 1$ and the moving boundary problem is transformed to a fixed boundary problem. The resulting PDE can be solved by Crank-Nicholson implicit method that leads to high accuracy and stability.

Simulation results of the EC concentration gradient along the SEI thickness direction are plotted in Fig. 4. The x-axis indicates the radial direction of the anode graphite particles or the thickness direction of the SEI layer. The EC concentration at the outer boundary of the SEI layer is equal to that in the electrolyte bulk, which is assumed to be constant. When the EC molecules slowly diffuse from the electrolyte to the graphite particle surface, the EC concentration in the SEI layer gradually decreases from the electrolyte-SEI interface to the SEI-particle interface. Initially, the EC concentration at the graphite particle surface is nearly zero. With time increased, the EC concentration at that place gradually

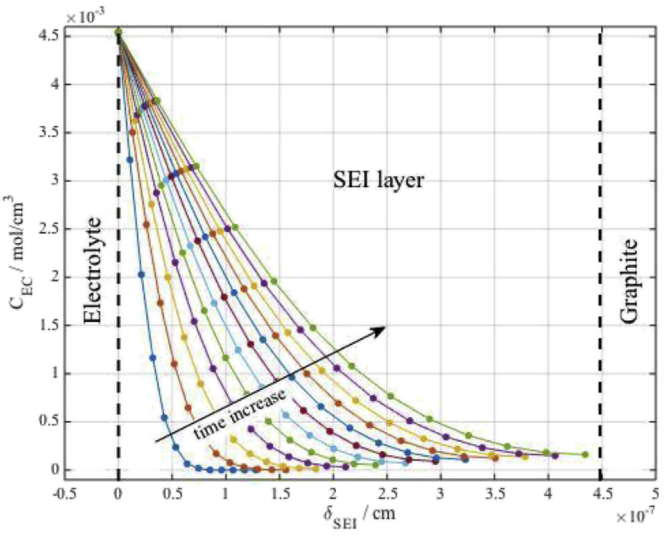

Fig. 4. Concentration of EC molecule in the SEI layer.

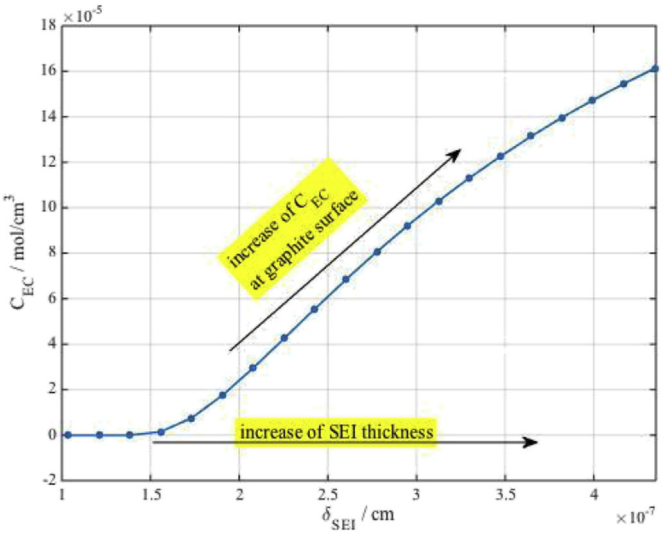

Fig. 5. EC concentration at the anode graphite particle surface.

increases and the thickness of the SEI grows as well.

The EC concentration at the anode graphite particle surface with respect to the SEI thickness is plotted in Fig. 5. It is shown that the EC concentration increases with the growth of the SEI thickness when the diffusion time prolonged. However, the slop of the curve decreases over time, which indicates that the EC concentration at the graphite surface tends to be balanced after a certain growth of SEI layer.

2.3. Effects of the side reaction

As discussed in the previous sections, the continuous occurrence of the side reaction through the prolonged cycles produces deposits that are accumulated as the 'bad SEI'. A schematic diagram of the SEI formation in a fresh and aged cell is depicted in Fig. 6 using the sandwich microcell model.

The yellow color areas in the aged cell indicate the deposits produced by the side reaction. The one around the particles are the SEI layer and the one in between the composite anode and the separator is the deposit layer. Some particles are partially or fully covered by the deposits. The partially covered particles still have contact with others, so electrons can flow. Circles marked with "X" represent the fully coated SEI, so particles are fully isolated from the electronic conduction. The other deposit is the layer formed between the composite anode and the separator.

Effects of the side reaction can be analyzed with respect to the reactants and the products. For reactants, the reaction consumes ions and electrolytes. The total amount of consumed ions is obtained by integration of reaction rate over the volume of the composite anode and time, which can be given in Equation (17):

$$q_{side}^{Li}(t) = \int_{x=0}^{\delta_-} \left(\int_{\tau=0}^{t} j_{side}^{Li}(x,\tau) d\tau \right) A dx \tag{17}$$

$q_{side}^{Li}(t)$ is the consumed lithium ions, δ_- is the thickness of the composite anode and A is the cross section area of the battery, respectively.

The decreasing rate of the volume fraction of electrolyte can be obtained by the ratio between volume fractions that is proportional to the integration of the side reaction rate over the thickness of the composite anode as follows:

$$\frac{\partial \varepsilon_e}{\partial t} = -\frac{\alpha \tilde{V}_e}{\delta_- F} \int_{x=0}^{\delta_-} j_{side}^{Li} dx \tag{18}$$

where $\tilde{V}_e$ is the molar volume of the electrolyte. α is the reaction coefficient of the EC that implies the molar ratio of EC over lithium ions in the side reaction.

Since the component of the SEI is a mixture of Li_2CO_3 and $(CH_2OCO_2Li)_2$ expressed in Equations (1) and (2), α is the coefficient indicating how many moles of electrolyte are consumed when 1 mol of lithium ion is consumed, which is set to 0.5 for the side reaction in Equation (1) and 1 for the side reaction in Equation (2). Under the assumption that both side reactions have the same reaction rate, an averaged value of 0.75 is used.

Correspondingly, the effective diffusivity of the lithium ions in electrolyte can be expressed by considering the change of electrolyte porosity.

$$D_e^{eff} = D_e \cdot \varepsilon_e^p \tag{19}$$

On the other hand, the products of the side reaction increase the thickness of the SEI layer and form a new deposit layer close to the separator on the anode composite electrode, whose rates can be described as in Equations (20) and (21):

$$\frac{\partial \delta_{SEI}}{\partial t} = -\frac{\tilde{V}_{SEI}}{2a_s F} j_{side}^{Li} \tag{20}$$

$$\frac{\partial \delta_{DL}}{\partial t} = -\frac{R_s \tilde{V}_{DL}}{2F} j_{side,x=\delta_-}^{Li} \tag{21}$$

where $\tilde{V}_{SEI}$ and $\tilde{V}_{DL}$ are the molar volumes of the SEI layer and the deposit layer respectively.

As results, the increasing rate of SEI and deposit layer resistance can be expressed as in Equations (22) and (23):

$$\Delta R_{SEI} = \delta_{SEI} / \kappa_{SEI} \tag{22}$$

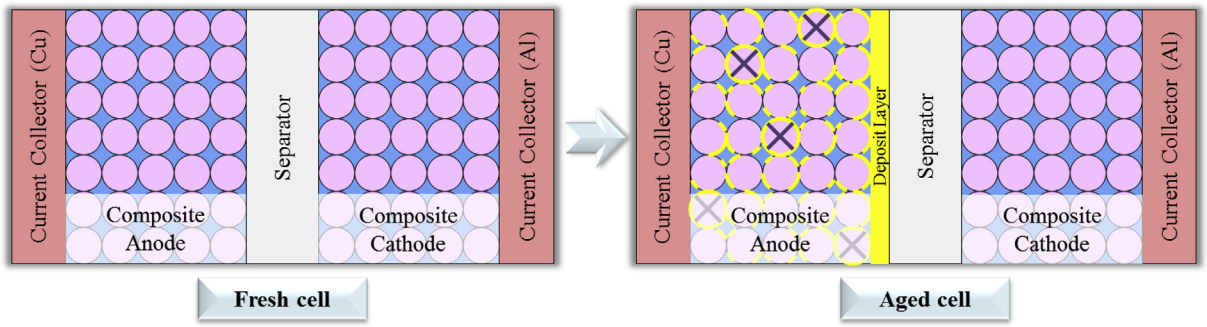

Fig. 6. Schematic diagram of the SEI formation in a microcell.

$$\Delta R_{DL} = \delta_{DL}/\kappa_{DL} \tag{23}$$

where κ_{SEI} and κ_{DL} are the ionic conductivity of the SEI and the deposit layer, respectively.

When the deposits clog the pores of the graphite particles, active material volume fraction decreases as follows:

$$\Delta\varepsilon_s = -k_s a_s \delta_{SEI} \tag{24}$$

where k_s is a dimensionless coefficient.

The effects of the side reaction are summarized in Table 4.

3. Experimental investigation

In order to cycle cells and collect data, a test station is constructed with a programmable power supply and an electronics load that are controlled by LabVIEW. The cells used for validations are pouch type lithium polymer batteries with following specifications;

- Chemistry: Cathode, $Li(MnNiCo)O_2$; Anode, surface modified graphite; Electrolyte, Gel polymer ($LiPF_6$+EC/DEC/EMC); Separator, Ceramic coated separator.
- Nominal capacity: 51 Ah.
- Operation range of the terminal voltage: 2.7V - 4.2V.
- Dimension: 14.7 mm × 280 mm × 185 mm.

The discharge data and the self-discharge data are acquired under different temperatures by an extra thermal chamber. The EIS data is also collected at a constant temperature of 25 °C and 50% of SOC.

3.1. Determination of temperature dependent parameters

There are two parameters that are temperature dependent in ROM, ion diffusivity in solid electrode particles and the contact ohmic film resistance. The experimental data and simulated results at 1C discharge from 0 °C to 60 °C for beginning of life of a cell are plotted in Fig. 7. The solid thin lines are the experimental data while the thick lines with markers are the simulation results obtained from the developed ROM. Both curves are in a fairly good match, accomplished by finding appropriate values for the two parameters at different temperatures.

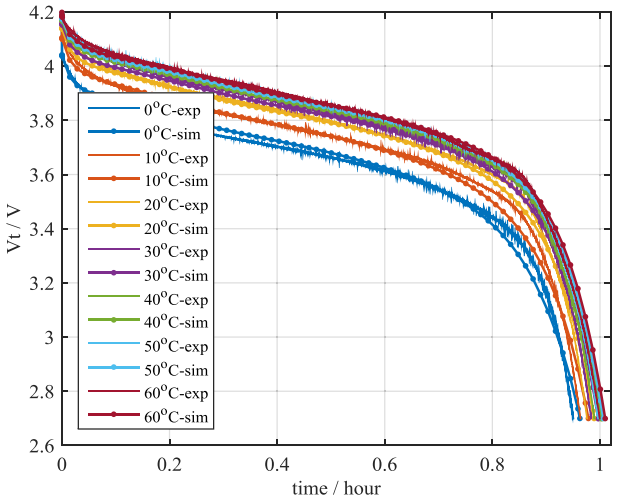

Fig. 7. 1C discharge curves at various temperatures.

The diffusion coefficient is expressed using the Arrhenius equation shown in (25), while the correlation of the film resistance and temperature is derived by an exponential empirical equation.

$$D_s = A_s \cdot \exp\left(-\frac{E_{a,s}}{RT}\right) \tag{25}$$

where A_s, $E_{a,s}$, R and T are the pre-factor, the activation energy, the universal gas constant and temperature, respectively.

The dependencies of the diffusion coefficient and film resistance on temperatures are depicted in Fig. 8. The markers are the

Table 4
Effects of the side reaction.

Side reaction	Effects on reactants and products	Effects on model parameters
Side reaction rate: $\left\|j_{side}^{Li}\right\|\uparrow$	Loss of lithium ion: $q_{side}^{Li}(t)\uparrow$ Loss of electrolyte: $\varepsilon_e\downarrow$	Capacity: $Q_{max}\downarrow$ Electrolyte volume fraction: $\varepsilon_e\downarrow$ Effective diffusivity: $D_e^{eff}\downarrow$
	SEI thickness: $\delta_{SEI}\uparrow$	SEI resistance and volume fraction: $R_{SEI}\uparrow$ and $\varepsilon_{SEI}\uparrow$ Active material volume fraction: $\varepsilon_s\downarrow$
	Deposit layer thickness: $\delta_{DL}\uparrow$	Ionic conductivity: $R_{DL}\uparrow$
Ohmic overpotential and terminal voltage: $V_T\downarrow$		

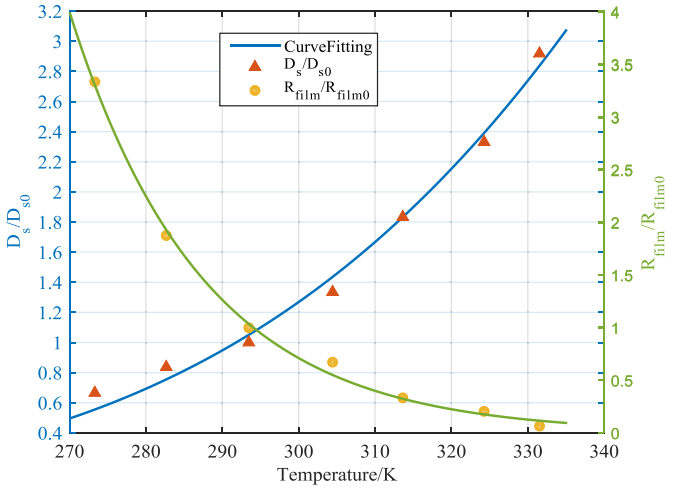

Fig. 8. Curve fitting of diffusion coefficient and film resistance at various temperatures.

corresponding parameters. The blue line and the green line are the fitted results of the diffusion coefficient and the film resistance, respectively. The diffusion coefficient increases while the film resistance decreases with the elevated temperature.

Since the SEI layer has high conductivity for lithium ions, but has very low permeability for the EC molecules, the rate of side reaction is predominantly determined by the availability of EC as reactants rather than the abundantly available lithium ions. Therefore, the diffusivity of the EC in the SEI layer that is also dependent upon temperature is particularly crucial for the rate of side reaction. The correlation of the diffusivity and temperature is expressed using the Arrhenius Equation (26):

$$D_{EC} = A_{EC} \cdot \exp\left(-\frac{E_{a,EC}}{RT}\right) \tag{26}$$

where A_{EC} and $E_{a,EC}$ are the pre-factor and the activation energy.

The values of the two coefficients in the equation are determined based on self-discharge characteristics obtained from experimental data. The terminal voltage measured over time at 0 °C, 25 °C and 40 °C, along with the fitting results of the EC diffusivity with respect to temperature are plotted in Fig. 9. The diffusivity increases as temperature increases.

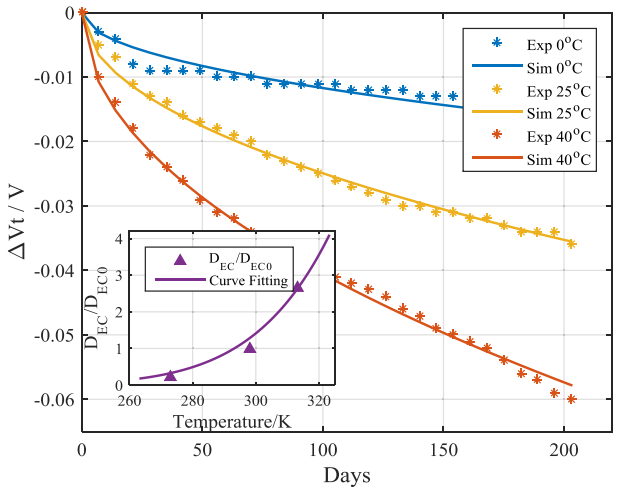

Fig. 9. Self-discharge data and fitted EC diffusivity over time.

3.2. Analysis of SEI resistance

In order to find the SEI resistance, impedance characteristics of cycled cells at 25 °C, 40 °C and 0 °C are measured using Electrochemical Impedance Spectroscopy (EIS) as plotted as dots in subplots 1, 2 and 3 in Fig. 10. The experimental data was fitted to an equivalent circuit model (EIS-ECM), so values of the electric components can be extracted. The impedance responses of ECM along with the extracted parameters are plotted as solid lines in subplots 1, 2 and 3 in Fig. 10.

The extracted SEI resistances are plotted in subplot 4 in Fig. 10. The solid markers and the corresponding error bars are the mean values and standard deviations, respectively. The radius of the semi-circle is mostly determined by SEI resistance that increased as a function of the number of cycles and ambient temperature. The SEI resistance severely increases at 40 °C, which is reflected as the change of semi-circles in subplot 2 and elevated red squares in subplot 4. By contrast, no obvious changes of the semi-circles are shown in subplot 1 and 2, as well as the yellow dots and blue triangles in subplot 4, which indicate less SEI formation at 25 °C and 0 °C.

4. Results and discussions

4.1. Simulation analysis at 25 °C

In order to analyze the changes of the aging related parameters inside of the battery over time, simulation results of the side reaction rate and the corresponding parameters are presented at 25 °C. The rate of side reaction at each grid points along the anode thickness direction and how the value changes with the increased cycle number are plotted in Fig. 11. The x-axis is the non-dimensional thickness of the anode. The interface between the current collector and the anode is located at $x = 0$ while the interface between the anode and the separator is located at $x = 1$. By examining each line along the x direction, it turns out that the side reaction rate is larger near the separator side, which accelerates the formation of the deposit layer in that area. With the cycle number increased, the side reaction is accumulated in the composite anode as the arrow indicates direction in the figure.

Correspondingly, the variation of the physical parameters discussed in the previous Section 2.3 are presented in Figs. 12 and 13, where the change of electrode volume fraction and SEI resistance at different grid points in anode and the change of electrolyte volume fraction and deposit layer resistance over different cycle numbers are plotted in Figs. 12 and 13, respectively. With the cycle number increased, the products of the side reaction is accumulated on the graphite particle surface, particularly near the separator because of higher side reaction rate caused by high ion concentration. Consequently, the SEI resistance, R_{SEI}, as well as the deposit layer resistance, R_{DL}, increases over time. Accordingly, the electrode volume fraction, ε_s, becomes less because of the isolation of the active material caused by the grown SEI layers, which is described by Equation (24). Similarly, the electrolyte volume fraction, ε_e, becomes less because of the side reaction that consumes the electrolyte.

4.2. Experimental validation at different temperatures

The effects of SOC range and charging C-rate on degradation have been discussed in Ref. [17]. The degradation is accelerated at high SOC range and charging C-rate has no clear effect on

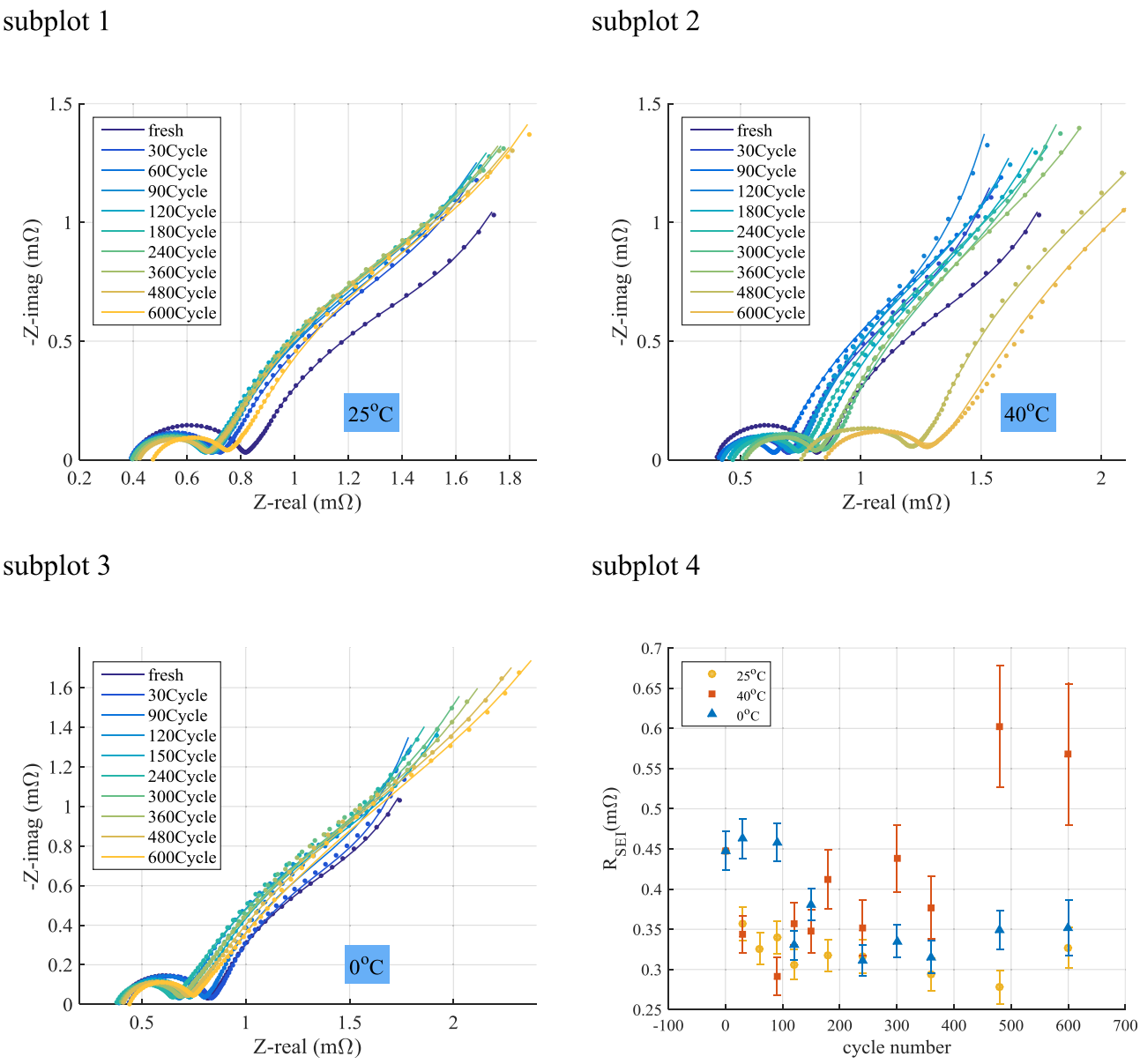

Fig. 10. Impedance characteristics and the SEI resistances at different temperatures.

degradation. However, temperature has the predominant effects on accelerating the cell degradation process. Therefore, the behavior of the aged cells at different temperatures is investigated in more details.

The experimental data includes SEI resistances extracted from EIS, and 0.2C discharge characteristics and cell capacity at different cycle numbers are compared with the simulated data. The changes of SEI resistance with the increase of cycle number at 0 °C, 25 °C and 40 °C are plotted in Fig. 14. The black markers connected by dash lines are simulation results, which tends to follow the experimental data with some deviations. Generally, the SEI resistance increases with the growth of cycle numbers, especially at high temperature. Increasing of SEI resistance that caused by the accumulated side reaction products causes power fade of the batteries.

The discharge characteristics of the degraded cells with 0.2C discharge current at 0 °C, 25 °C and 40 °C are shown in Figs. 15 and 16. The solid thin lines are the experimental data at 30, 300 and 600 cycles and the thick lines with markers are the simulation results for up to 1500 cycles. As the number of cycles increases, the terminal voltage decreases and the discharge time becomes shorter due to capacity fade. The simulated terminal voltage tends to follow the experimental data for the beginning and middle of the cycling at 25 °C and 40 °C while the discrepancy occurs at 0 °C, which is caused by large ohmic overpotential at low temperature. At the end of the cycling, the simulated voltage matches pretty well with the experimental data for 30, 300 cycles. However, there are some deviations appear at 600 cycles that are caused by inaccurate estimation of capacity. Since the side reactions accumulated in a battery is not increased linearly with cycle number, the algorithm of capacity estimation involves a nonlinear relationship between the side reaction and the cycle number. With the cycle number increased, the complexity of tracking the nonlinearity increased, which makes the capacity estimation error increased.

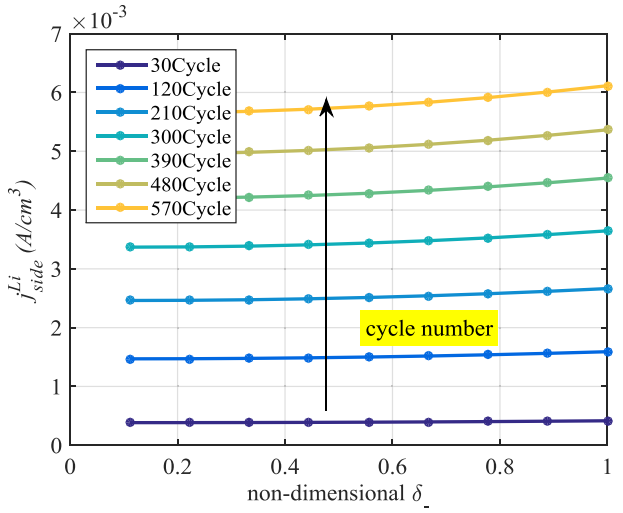

Fig. 11. Accumulated side reaction rate along the anode thickness direction.

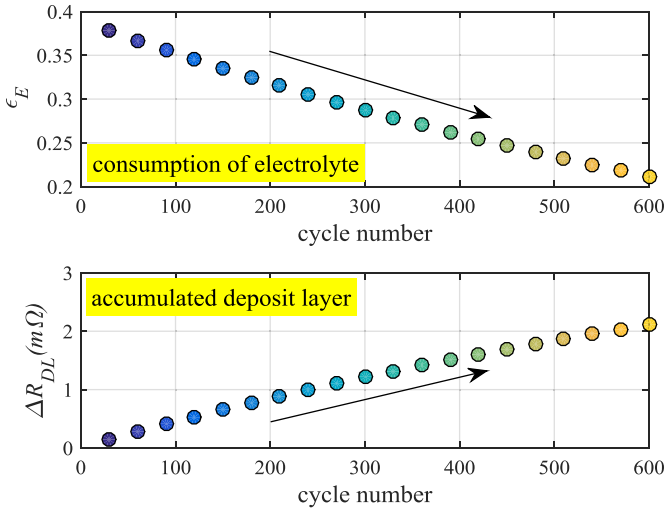

Fig. 13. Change of electrolyte volume fraction and deposit layer resistance with increasing cycle number.

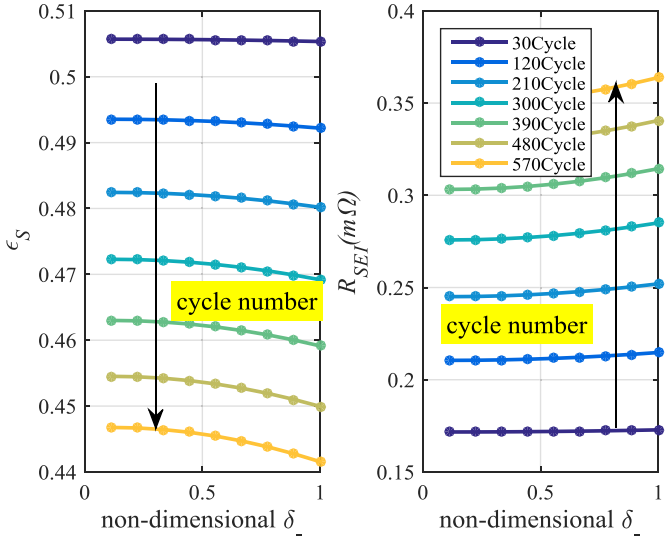

Fig. 12. Change of electrode volume fraction and SEI resistance along the anode thickness direction.

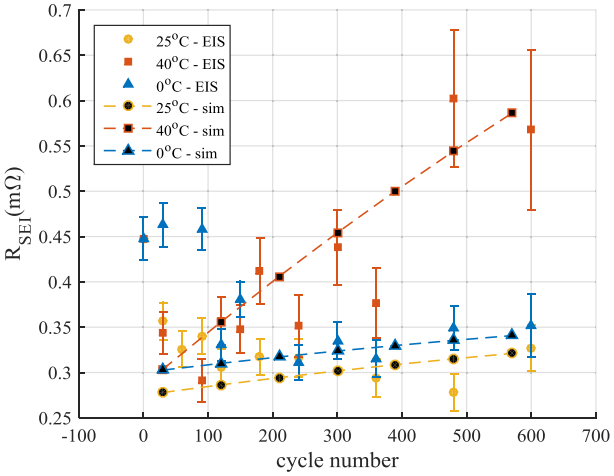

Fig. 14. Change of SEI resistance with increasing cycle number.

In order to compare the performance of the model with respect to capacity fade, the capacity is measured at discharging with 0.2C rate for every 30 cycle at 0 °C, 25 °C and 40 °C. For better analysis, a relative capacity is introduced and defined as the percentage of the aged cell capacity over the fresh cell capacity as shown in equation (27). The relative capacity between the simulated and experimental data is compared up to 600 cycles in Fig. 17 and then predicted up to 1500 cycles at different temperatures.

$$Q_{rel} = \frac{Q_{aged}}{Q_{fresh}} \times 100\% \tag{27}$$

More severe degradation is observed and estimated at higher and lower ambient temperatures compared to the room temperature operation, which is shown as the capacity of the cell at 0 °C and 40 °C decreases faster than the cell at 25 °C. At higher temperature range, EC molecules and lithium ions have better mobility, which results in intense chemical reaction and diffusion not only for the main reaction but also for the side reaction. Hence, the degradation that caused by the side reaction is more aggressive at elevated temperature range. At lower temperature range, the transport losses are higher than that at high temperature range. Consequently, more heat is generated inside of the battery during cycling though the ambient temperature is low, which also leads to more degradation. The simulation results tend to follow the experimental data as shown in Fig. 17, where the capacity fade at 900 and 1500 cycles are predicted. The error percentage of the relative capacity estimation is calculated in Equation (28) and depicted in Fig. 18, which shows that the deviation of the simulation results from the experimental data is less than 5%.

$$error = \frac{Q_{rel,sim} - Q_{rel,\exp}}{Q_{rel,\exp}} \times 100\% \tag{28}$$

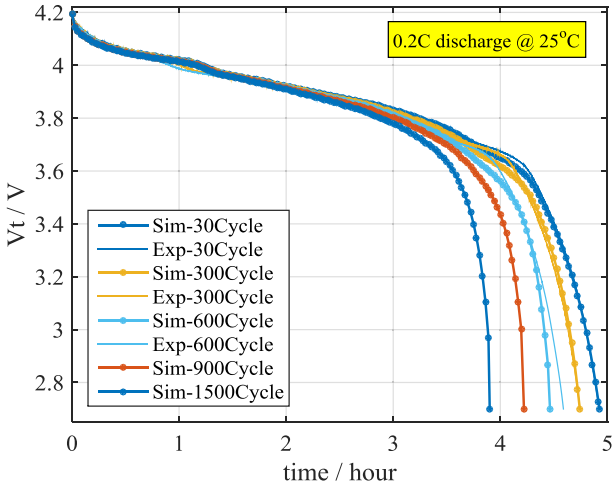

Fig. 15. Discharge characteristics of the degraded cell at different number of cycles at 25 °C.

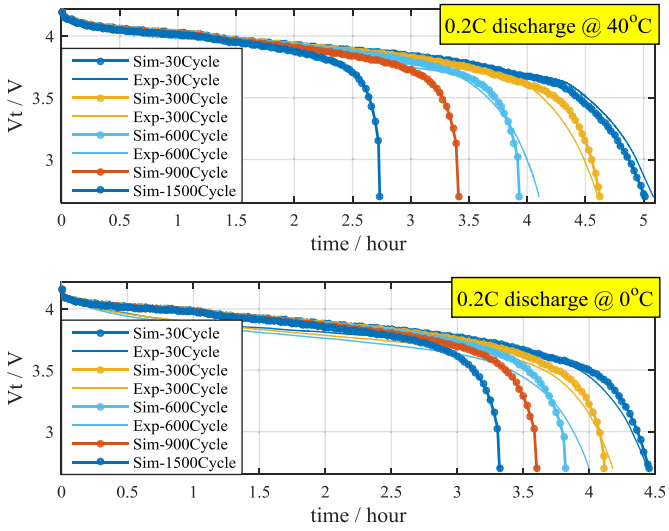

Fig. 16. Discharge characteristics of the degraded cell at different number of cycles at 40 °C and 0 °C.

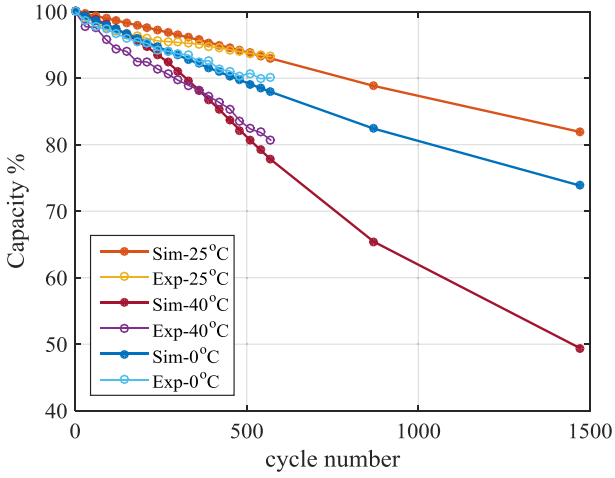

Fig. 17. Relative capacity at different temperatures.

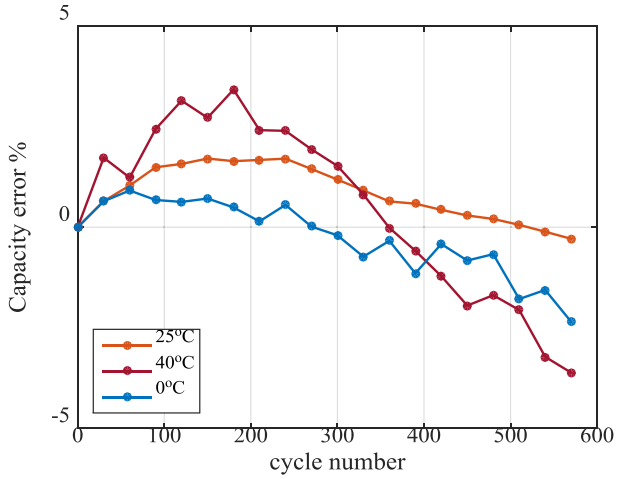

Fig. 18. Error of the relative capacity estimation at different temperatures.

5. Conclusion

Review of papers and experimental studies have revealed that the side reaction is the main cause for performance degradation of the lithium ion battery. The side reaction is mathematically described by modifying the Butler-Volmer equation and the corresponding degradation processes are modeled based on physical principles. The degradation model is incorporated into the previously developed ROM. The integrated model is then validated against experimental data obtained from a large format pouch type of Li [MnNiCo]O_2/Graphite cells.

Main accomplishments and findings are summarized as follows:

- Improvement of the porous electrode model by adding the mass balance of electrolyte solvent,
- Modification of the exchange current density as a function of lithium ion concentration and the EC concentration on the electrode particle surfaces,
- Temperature dependence of the diffusion coefficients of the lithium ion in electrode particles and the EC molecules in electrolyte,
- Analysis of parameter sensitivities at 25 °C
- Incorporation the aging model in the ROM and its experimental validation at different temperatures that include SEI resistance from EIS measurements, discharge characteristics and relative capacity from the cycling data,
- Cycling at elevated temperature and low temperature has significantly accelerated the degradation process. More severe capacity fade is found in high temperature range,
- Error of prediction of capacity fade is less than 5% up to 600 cycles.

Future work will include parameter identification of the model for the battery beginning of life and for the battery end of life.

Acknowledgments

The financial support of Hyundai Motor Company is gratefully acknowledged.

Appendix

Parameters of the ROM [2].

Category	Parameter	Negative electrode	Separator	Positive electrode	unit
Geometry and volume fractions	Thickness, δ	52×10^{-4}	30×10^{-4}	62×10^{-4}	cm
	Particle radius, R_s	0.85×10^{-4}		0.85×10^{-4}	cm
	Active material volume fraction, ε_s	0.58		0.5	
	Polymer phase volume fraction, ε_p	0.048	0.5	0.11	
	Conductive filler volume fraction, ε_f	0.04		0.06	
	Porosity, ε_e	0.332	0.5	0.33	
Li^+ concentrations	Stoichiometry at 0% *SOC*: $x_{0\%}$, $y_{0\%}$	0.2004		0.996	
	Stoichiometry at 100% *SOC*: $x_{100\%}$, $y_{100\%}$	0.8885		0.3115	
	Average electrolyte concentration, c_e	1.2×10^{-3}	1.2×10^{-3}	1.2×10^{-3}	mol cm^{-3}
	Exchange current density coefficient, k_{i0}	13.2		6.79	A cm^{-2}
Kinetic and transport properties	Charge-transfer coefficient, α_a, α_c	0.5, 0.5	0.5, 0.5		
	Solid phase diffusion coefficient, D_s	0.67×10^{-12}		7.4×10^{-12}	$cm^2\ s^{-1}$
	Solid phase conductivity, σ	1		0.01	S cm^{-1}
	Electrolyte phase Li^+ diffusion coefficient, D_e	3×10^{-6}	3×10^{-6}	3×10^{-6}	$cm^2\ s^{-1}$
	Bruggeman's porosity exponent, p	1.5	1.5	1.5	
	Electrolyte phase ionic conductivity, κ	$15.8c_e$ exp $(-13472c_e^{1.4})$		$15.8c_e$ exp $(-13472c_e^{1.4})$	S cm^{-1}
	Li^+ transference number, t_+^0	0.363	0.363	0.363	

Parameters of the degradation model.

Parameter	Value	Source
EC diffusion coefficient D_{EC} ($cm^2\ s^{-1}$)	1.5×10^{-21} at 0 °C 6.8×10^{-21} at 25 °C 18×10^{-21} at 40 °C	Optimized by comparing simulation to the self-discharge data
equilibrium potential of side reactions, $U_{eq,\ side}$ (V)	0.4	Optimized by comparing simulation to the experimental data
molar volume of SEI, $\bar{V}_{SEI}$ (cm^3/mol)	2	Obtained by assuming the initial thickness of SEI is 2 nm
ionic conductivity of SEI, κ_{SEI} (S cm^{-1})	2.5×10^{-8}	Optimized by comparing simulation to the SEI resistance obtained from EIS
isolation rate of active anode materials due to SEI, k_{iso}	45.7	Optimized by comparing simulation to measured capacity fade
molar volume of DL, $\bar{V}_{DL}$ (cm3/mol)	7560	Obtained from literature [17]
ionic conductivity of DL, κ_{DL} (S cm^{-1})	1×10^{-3}	Optimized by comparing simulation to the terminal voltage under cycling
molar volume of electrolyte, $\bar{V}_e$ (cm3/mol)	252	Optimized by comparing simulation to the terminal voltage under cycling

References

[1] L. Gao, S. Liu, R.A. Dougal, IEEE Trans. Compon. Packag. Technol. 25 (3) (2002) 495–505.
[2] Y. Zhao, S.Y. Choe, J. Electrochim. Acta 164 (2015) 97–107.
[3] J. Vetter, P. Novak, M. Wagner, C. Veit, K. Moller, J. Besenhard, M. Winter, M. Wohlfahrt-Mehrens, C. Vogler, A. Hammouche, J. Power Sources 147 (2005) 269–281.
[4] M. Pinson, M. Bazant, J. Electrochem. Soc. 160 (2013) A243–A250.
[5] D. Aurbach, M. Levi, E. Levi, A. Schechter, J. Phys. Chem. B 101 (1997) 2195–2206.
[6] D. Aurbach, J. Power Sources 89 (2000) 206–218.
[7] R. Fu, S.Y. Choe, V. Agubra, J. Fergus, J. Power Sources 261 (2014) 120–135.
[8] M. Broussely, S. Herreyre, P. Biensan, P. Kasaztejna, K. Nechev, R. Staniewicz, J. Power Sources 97–98 (2001) 13–21.
[9] P. Ramadass, B. Haran, R. White, B. Popov, J. Power Sources 123 (2003) 230–240.
[10] S. Santhanagopalan, Q. Zhang, K. Kumaresan, R. White, J. Electrochem. Soc. 155 (2008) A345–A353.
[11] V. Ramadesigan, K. Chen, N. Burns, V. Boovaragavan, R. Braatz, V. Subramanian, J. Electrochem. Soc. 158 (2011) A1048–A1054.
[12] G. Prasad, C. Rahn, J. Power Sources 232 (2013) 79–85.
[13] P. Ramadass, B. Haran, P. Gomadam, R. White, B. Popov, J. Electrochem. Soc. 151 (2004) A196–A203.
[14] H. Ploehn, P. Ramadass, R. White, J. Electrochem. Soc. 151 (2004) A456–A462.
[15] G. Sikha, B. Popov, R. White, J. Electrochem. Soc. 151 (2004) A1104–A1114.
[16] M. Safari, M. Morcrette, A. Teyssot, C. Delacourt, J. Electrochem. Soc. 156 (2009) A145–A153.
[17] R. Fu, S.Y. Choe, V. Agubra, J. Fergus, J. Power Sources 278 (2015) 506–521.
[18] K. Edström, M. Herstedt, D. Abraham, J. Power Sources 153 (2006) 380–384.
[19] H. Bryngelsson, M. Stjerndahl, T. Gustafsson, K. Edström, J. Power Sources 174 (2007) 970–975.
[20] P. Verma, P. Maire, P. Novák, J. Electrochem. Acta 55 (2010) 6332–6341.
[21] M. Doyle, T. Fuller, J. Newman, J. Electrochem. Soc. 140 (1993) 1526–1533.
[22] J. Yao, W. Liu, Z. Chen, Math. Probl Eng. (2013).